Contents lists available at ScienceDirect

Materials Today Bio

journal homepage: www.journals.elsevier.com/materials-today-bio

NIR-triggered and glucose-powered hollow mesoporous Mo-based single-atom nanozymes for cascade chemodynamic diabetic infection therapy

Jingwei Wang[a,b,1], Yin Yu[c,1], Lingzhi Chen[b], Jiaqi Yu[a], Xiaoying Jin[a], Runmin Zeng[b], Xiaomin Luo[a], Yanguang Cong[a], Guangxian Xu[a], Jianglin Zhang[b,**], Xueqin Huang[a,***], Jiang Pi[a,*]

[a] *Guangdong Provincial Key Laboratory of Medical Immunology and Molecular Diagnostics, The First Dongguan Affiliated Hospital, School of Medical Technology, Guangdong Medical University, Dongguan, Guangdong, 523000, China*
[b] *College of Pharmacy, The Second Clinical Medical College (Shenzhen People's Hospital), The Fifth Affiliated Hospital, Jinan University, Guangzhou, Guangdong, 510632, China*
[c] *School of Chemistry and Chemical Engineering Nanjing University of Science and Technology, Nanjing, Jiangsu, 210094, China*

ARTICLE INFO

Keywords:
Single-atom nanozymes
Diabetic infection
Cascade catalytic
Antibacterial activity
Wound healing

ABSTRACT

Diabetic infections/wounds remain to be a threatening challenge as it seriously leads to lower limb amputation with endless pains and subsequent high economic/psychosocial costs. The exceptional peroxidase-like activity of single-atom nanozymes (SAzymes) holds great promise for chemodynamic therapy (CDT) of diabetic infection, but is extremely restricted by the near-neutral pH and insufficient H_2O_2 levels in physiological conditions. Herein, we innovated a hollow mesoporous molybdenum single-atom nanozyme (HMMo-zyme) featured with catalytic activity, photothermal performance and drug delivery properties for more effective antibacterial therapeutic in diabetic conditions. The glucose oxidase (GOx) was encapsulated into HMMo-zyme with phase-change material (PCM) to form HMMo/GOx@P system, which could be controllably disassembled by near-infrared ray (NIR) to trigger cascade CDT toward bacterial infections. The results revealed that the release of GOx accelerated by NIR could facilitate the continuous conversion of glucose (Glu) into gluconic acid, accompanied by a sharply decrease in pH to establish a low-pH environment that notably enhanced the catalytic activity of HMMo-zyme, which subsequently drives the conversion of generated H_2O_2 into toxic hydroxyl radicals (·OH) for amplified anti-bacterial treatment. As a proof of the concept, this NIR-assisted HMMo/GOx@P strategy could efficiently inhibit/kill bacteria and suppress tissue inflammations, thereby accelerating the wound healing processes both in *in vitro* and *in vivo* diabetic infection models. This study provides a novel strategy that may serve as a promising alternative for antibiotic therapeutics against diabetic infection, thus holding promise for more effective diabetic infection treatment manipulating Mo-based SAzymes.

1. Introduction

Diabetes mellitus, an increasingly prevalent chronic metabolic disease characterized by prolonged hyperglycemia, always leads to diabetic infections and wounds that may result in lower limb amputation to severely threaten human health [1,2]. Moreover, inadequate infection control and wound healing can exacerbate inflammatory responses and loss of skin integrity to create an ideal environment for bacterial growth, potentially leading to systemic infections [3–6]. Although plenty of efforts have been made to facilitate the discovery/development of antibiotics for bacterial infection therapeutics in diabetes patients, the use of antibiotics non-specifically impair human microbial community, which gives rise to metabolic disorders to worse diabetes conditions [7,8]. And the misuse of antibiotics also lead to the emergence of drug-resistant

---

* Corresponding author.
** Corresponding author.
*** Corresponding author.
E-mail addresses: Zhang.jianglin@szhospital.com (J. Zhang), xqhuang@jnu.edu.cn (X. Huang), jiangpi@gdmu.edu.cn (J. Pi).

[1] These authors contributed equally to this work.

https://doi.org/10.1016/j.mtbio.2025.101557
Received 2 January 2025; Received in revised form 25 January 2025; Accepted 4 February 2025

strains, posing significant challenges for both patients and attending physicians, which thus require effective antibiotic-free therapeutics against diabetic infections.

Taking the advantages of functional materials and nanotechnology advances[9–13], nanomaterial-assisted therapeutic strategies have received tremendous attention in recent years. The advent of functional nanomaterials offers new opportunities for the treatment of bacterial infections, serving as antibiotic delivery systems or bioactive dressings, to control inflammation and promote wound healing, as well as improve the course and prognosis of infections [14–17]. Based on Fenton or Fenton-like reaction[18–22], chemodynamic therapy (CDT) is developed to produce large amounts of hydroxyl radicals (·OH) to kill pathogens via the spontaneous activation by an endogenous stimulus, which can be intelligently controlled by nanotechnology. As nanoscale entities with enzyme mimic activities, nanozymes are capable of catalyzing hydrogen peroxide to ·OH via a Fenton-like reaction, thus enabling effective CDT against infections. However, most of traditional nanozymes are challenging to fewer active site exposure and lower atomic utilization efficiency in the process of catalytic reaction. In contrast, single-atom nanozymes (SAzymes) are considered as ideal candidates due to their well-defined electronic and geometric structures, as well as their superior selectivity and maximum atomic utilization efficiency (100 %) [23,24]. These properties and characteristics allow it promising as a regulable system that can activate the “on-off” through the inherent characteristics of the bacteria-infected microenvironment. More interestingly, SAzymes with unique structures and versatile chemical properties may also be turned on in response to various external stimuli [25–28]. For example, functional SAzymes with photothermal response characteristics can be rationally designed for CDT-enabled therapeutics, which can be intelligently triggered and controlled by NIR irradiation [29,30]. But how to actively engineer SAzymes for manipulating NIR-mediated chemodynamic therapy to achieve antibiotic-free therapeutics in diabetic infections/wounds remains a substantial challenge.

SAzymes are preferred to execute their peroxidase-like activity in acidic conditions (pH 3–6) by pre-absorption of H^+ and base-like decomposition of H_2O_2[31–33], which introduce natural restrictions for their biological uses as most physiological conditions are alkalescent, limiting the efficacy of SAzymes in diabetic wounds healing. Moreover, the concentration of physiological H_2O_2 is also inadequate to support highly efficient ·OH production by nanozyme catalysis, posing substance limitation for SAzymes-mediated CDT therapeutic in diabetic wound healing [34,35]. Based on our expertises on nanotechnology [36–39], we fabricated a hollow mesoporous molybdenum based single-atom nanozymes (HMMo-zyme) with peroxidase-like activity and photothermal performance for cascade CDT to simultaneously break the physiological pH and H_2O_2 limitations in diabetic wounds. Considering the high glucose environment in diabetic wounds, HMMo-zyme was developed as a vehicle for GOx encapsulation, followed by the conjugation with temperature-responsive phase-change material tetradecanol (PCM) as a pore blocker to form a novel HMMo/GOx@P nanozyme antibacterial system (Scheme 1A). Under near-infrared irradiation, the local heating caused by HMMo/GOx@P induced phase transition of PCM to precisely regulate GOx release, which continuously catalyzed glucose to gluconic acid and H_2O_2. This strategy not only drops pH in diabetic wound microenvironment to facilitate peroxidase-like activity of HMMo-zyme, but also supplements H_2O_2 substrate for *in situ* generation of toxic ·OH on bacteria surface, leading to highly efficient CDT sterilization under physiological conditions (Scheme 1B). Together, this work offers a novel approach for developing nanozyme-assisted CDT cascade therapy with broad-spectrum antibacterial capabilities for diabetic wounds treatment, thus providing novel promise for more effective diabetic infections/wounds treatment.

2. Materials and methods

2.1. Materials and reagents

2-Methylimidazole ($C4H_6N_2$, 98.0 %), molybdenyl acetylacetonate (MoO_2 $(acac)_2$), tetradecyl alcohol (PCM), tannic acid, 3,3,5,5-tetramethylbenzidine (TMB, >99 %) were purchased from Aladdin Biochem Technology Co., Ltd. (Shanghai, China). Zinc(II) nitrate hexahydrate ($Zn(NO_3)_2 \bullet 6H_2O$, 99.0 %), methanol (CH_3OH, AR), hydrogen peroxide (H_2O_2, 30 % aqueous solution), and terephthalic acid (99 %) were bought from Sinopharm Chemical Reagent Co., Ltd. (Shanghai, China). Glucose oxidase (GOx) was ordered from Sigma-Aldrich (St. Louis, USA). Glucose (Glu) and methyl red (95 %) were obtained from Macklin

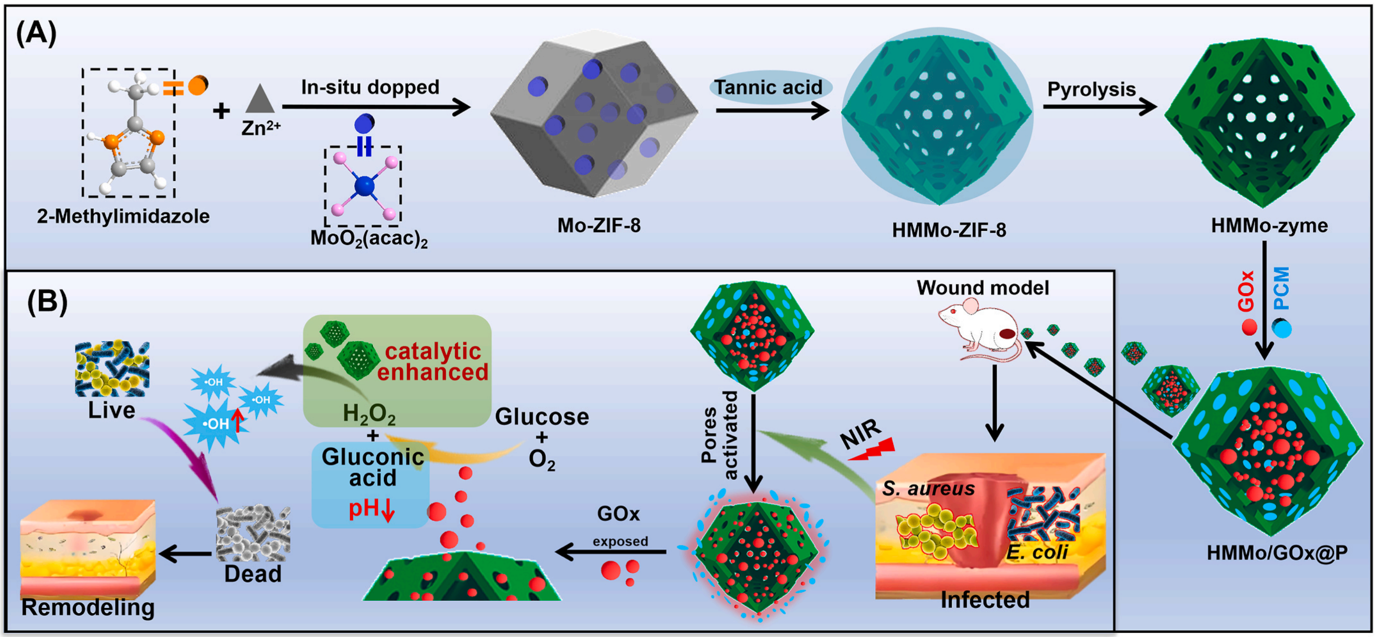

Scheme 1. (A) The fabricated process for the HMMo-zyme with temperature-responsive phase-change material tetradecanol (PCM) and glucose oxidase (HMMo/GOx@P). (B) Schematic illustration of NIR triggering, GOx release and cascade catalysis in the infected wound, and its application to *in situ* production of toxic ·OH on bacteria surface for CDT sterilization.

Biochemical Co., Ltd. (Shanghai, China). Live/Dead bacLight bacterial viability kits and cell counting Kit-8 (CCK-8) were bought from Thermo Fisher Scientific Inc. (Waltham, USA). Dulbecco's Modified Eagle's Medium (DMEM), fetal bovine serum (FBS), phosphate buffered saline (PBS), penicillin, streptomycin and trypsin were purchased from Gibco BRL (Gaithersburg, USA). Human umbilical vein endothelial cell (HUVEC) was received from the Cell Bank of Type Culture Collection of the Chinese Academy of Sciences (Shanghai, China). *Staphyloccocu saureus* (*S. aureus*, ATCC25923) and *Escherichia coli* (*E. coli*, ATCC 25922) were purchased from fuxiang Biotechnology Co., Ltd. (Shanghai, China). All reagents were purchased from commercial sources and used without any further purification.

2.2. Preparation of HMMo-zyme and HMMo/GOx@P

Zeolitic Imidazolate Framework-8-confined Mo sources (Mo-ZIF-8) were prepared in a "host-guest" strategy [40]. Specifically, 2-methylimidazole (3700 mg) was dissolved in 80 mL of methanol under ultrasound for 30 min, and designated as Solution A. $Zn(NO_3)_2 \bullet 6H_2O$ (1666 mg) and molybdenum acetylacetonate ($MoO_2(acac)_2$, 130 mg) were dissolved in 40 mL of methanol with sonication for 30 min, forming Solution B. Solution B was then added to Solution A and stirred at room temperature for 12 h. The resulting Mo-ZIF-8 was centrifuged at 8500 rpm, washed three times with methanol, and freeze-dried for further use.

For the synthesis of HMMo-zyme, 100 mg of Mo-ZIF-8 was dispersed in 20 mL of ultrapure water and subjected to ultrasound for 30 min at room temperature. After forming a homogeneous dispersion, 1.25 mL of tannic acid (25 mg/mL) was added to the mixture and stirred at room temperature for 10 min. The resulting HMo-ZIF-8 was centrifuged at 12000 rpm, washed three times with ultrapure water, and freeze-dried for 12 h. Finally, pyrolysis is performed at 900 °C for 3 h under a flowing N_2 atmosphere, where HMo-ZIF-8 undergoes a controlled decomposition without unnecessarily reactions with oxygen, so as not to affect the formation and properties of product. The formation of black powders demonstrated the successful fabrication of HMMo-zyme.

To obtain the HMMo/GOx@P, the GOx (4 mL, 2 mg/mL) was incubated with HMMo-zyme (4 mL, 1 mg/mL) at room temperature overnight, and the excess GOx was washed to remove. Then, the as-prepared HMMo/GOx was redispersed in 20 mL of ultrapure water, and mixed with the PCM, followed by heating to 42 °C until the PCM was fully dissolved. After centrifugation, the supernatant was collected to obtain the HMMo/GOx@P. The drug loading capacity and encapsulation efficiency of GOx in HMMo-zyme were calculated by BCA testing kit according the following formulas:

$$\text{Encapsulation ratio (\%)} = (1 - W_r/W_a) \times 100 \text{ (Equation-1)}$$

$$\text{Loading ratio (\%)} = (W_e/W_t) \times 100 \text{ (Equation-2)}$$

Here, W_a (mg) and W_r (mg) represent GOx added to the solution and remained in the supernatant after encapsulation, respectively. W_e (mg) and W_t (mg) represent GOx encapsulated in the system and total weight of drug-containing system, respectively. Notice: $W_e = W_a - W_r$.

2.3. NIR-regulated in vitro release of GOx

To evaluate the release performance of GOx *in vitro*, 10 mg of HMMo/GOx@P were suspended in PBS, and then dialyzed using a dialysis membrane (MWCO 5000). The sample was shaken at 25 °C, 37 °C or 42 °C in dark, respectively. At predetermined time points, 2 mL of solution was taken away and replenished with 2 mL of fresh PBS. The cumulative release of GOx was detected and calculated by BCA testing kit according to the formulas as shown above. To investigate the NIR-regulated GOx release, HMMo/GOx@P was irradiated with NIR laser (1.5 W/cm^2) for 5 min, and the amount of GOx released at predetermined time points was observed and calculated as described above.

2.4. Cascade reaction of HMMo/GOx

HMMo/GOx can convert Glu into H_2O_2 and gluconic acid, resulting in the decrease of pH in diabetic infected wounds. To study the catalytic activity of HMMo/GOx, the different reaction systems were evaluated as follows: (I) PBS, (II) Glu, (III) HMMo/GOx, (IV) Glu + HMMo-zyme, (V) Glu + GOx, and (VI) Glu + HMMo/GOx. The concentrations of Glu, GOx, HMMo-zyme and HMMo/GOx were 5 mM, 5 μg/mL, 100 μg/mL and 100 μg/mL, respectively. The reaction was conducted at 37 °C for 3 h, after which the pH values of each group were measured using methyl red.

In addition, the decomposition of Glu produced H_2O_2, which in turn served as substrate for the catalytic cascade reaction of HMMo-zyme. The catalytic activity of HMMo-zyme was evaluated by using TMB as indicator, whose oxidized product (oxTMB) is a strikingly blue charge transfer complex with a maximum absorption peak at 652 nm [38]. The TMB reactions were performed as follows: (I) PBS, (II) Glu, (III) HMMo + Glu, (IV) Glu + GOx, (V) Glu + HMMo/GOx, and (VI) Glu + HMMo/GOx + NIR (1.5 W/cm^2 5min), respectively. The concentrations of HMMo-zyme, HMMo/GOx, GOx, Glu, and TMB were 100 μg/mL, 100 μg/mL, 5 μg/mL, 5 mM, and 1 mM, respectively. The reaction was conducted at 37 °C for 3 h, after which the color and the absorbance changes in each group were observed and measured.

2.5. Antibacterial activity of HMMo/GOx@P in vitro

E. coli and *S. aureus* (10^7 CFU/mL) were treated with (I) PBS, (II) HMMo-zyme, (III) HMMo-zyme + NIR, (IV) HMMo/GOx@P + Glu, (V) HMMo/GOx + Glu, and (VI) HMMo/GOx@P + Glu + NIR (1.5 W/cm^2 5 min), and then incubated at 37 °C under shaking (180 rpm) for 5 h. The concentrations of HMMo-zyme, HMMo/GOx, HMMo/GOx@P, and Glu were 100 μg/mL, 100 μg/mL, 100 μg/mL, and 5 mM, respectively. The bacterial suspensions were diluted 10,000 times, spread on a solid medium, and cultured for 24 h at 37 °C. Finally, the amount of colony was counted to evaluate the antibacterial effects of each group.

To visually demonstrate antibacterial effect of cascade strategy, the treated bacteria were centrifuged, washed with PBS, and fixed with 2.5 % glutaraldehyde at 4 °C for 2 h. The fixed bacteria were then dehydrated sequentially with 30 %, 50 %, 70 %, 80 %, 90 %, 95 %, and 100 % ethanol [41]. Finally, the dried or damage bacteria were fixed and observed using a scanning electron microscope (SEM). For live/dead fluorescence imaging of bacteria, the treated bacteria were stained with propidium iodide (PI) (3 μL, 20 mM) and SYTO 9 (3 μL, 3 mM) for 30 min at room temperature in dark, where SYTO-9 penetrates in all intact and damage bacterial membranes with green color and PI could only label damage cell membranes with red color [42]. After staining, the bacteria were washed three times to remove excess dyes and imaged using a laser confocal fluorescence microscope (CLSM).

2.6. Antibacterial performance of HMMo/GOx@P in vivo

BALB/c mice (aged 6–8 weeks, male) were housed in a climate- and light-controlled environment with unrestricted access to food and water. Firstly, mice were injected intraperitoneally with streptozotocin (STZ) (150 mg/kg) after fasting for 12 h to establish a diabetic model. The model was considered successful when the mice lost weight and increased their blood Glu levels by more than 16.8 mmoL/L over two weeks [43,44]. To evaluate the antibacterial efficacy of HMMo/GOx@P *in vivo*, an infected diabetic wound model was established by cutting 6 mm wounds on the backs of the mice, followed by the injection of *S. aureus* (3×10^7 CFU/mL, 50 μL) into the wounds. After 24 h, the mice were randomly divided into six groups to perform different treatments: (I) PBS, (II) HMMo-zyme, (III) HMMo-zyme + NIR, (IV) HMMo/GOx@P, (V) HMMo/GOx, and (VI) HMMo/GOx@P + NIR (1.5 W/cm^2 5 min). Wounds were measured and photographed every two day after administration. On day seven, the infected wounds were homogenized, suspended in 1 mL of sterile saline, and incubated at 37 °C for 24 h, followed by bacterial analysis using the plate colony method. After treatment, wound tissue samples were collected for Hematoxylin-Eosin (H&E) and Masson trichrome staining to determine wound repair effect. Furthermore, the immunofluorescent staining of interleukin-6 (IL-6) was conducted to observe the inflammation at the wound sites. All animal procedures comply with institutional Guide for Care and Use of Laboratory Animals from the animal ethics committee (Shenzhen People’s Hospital).

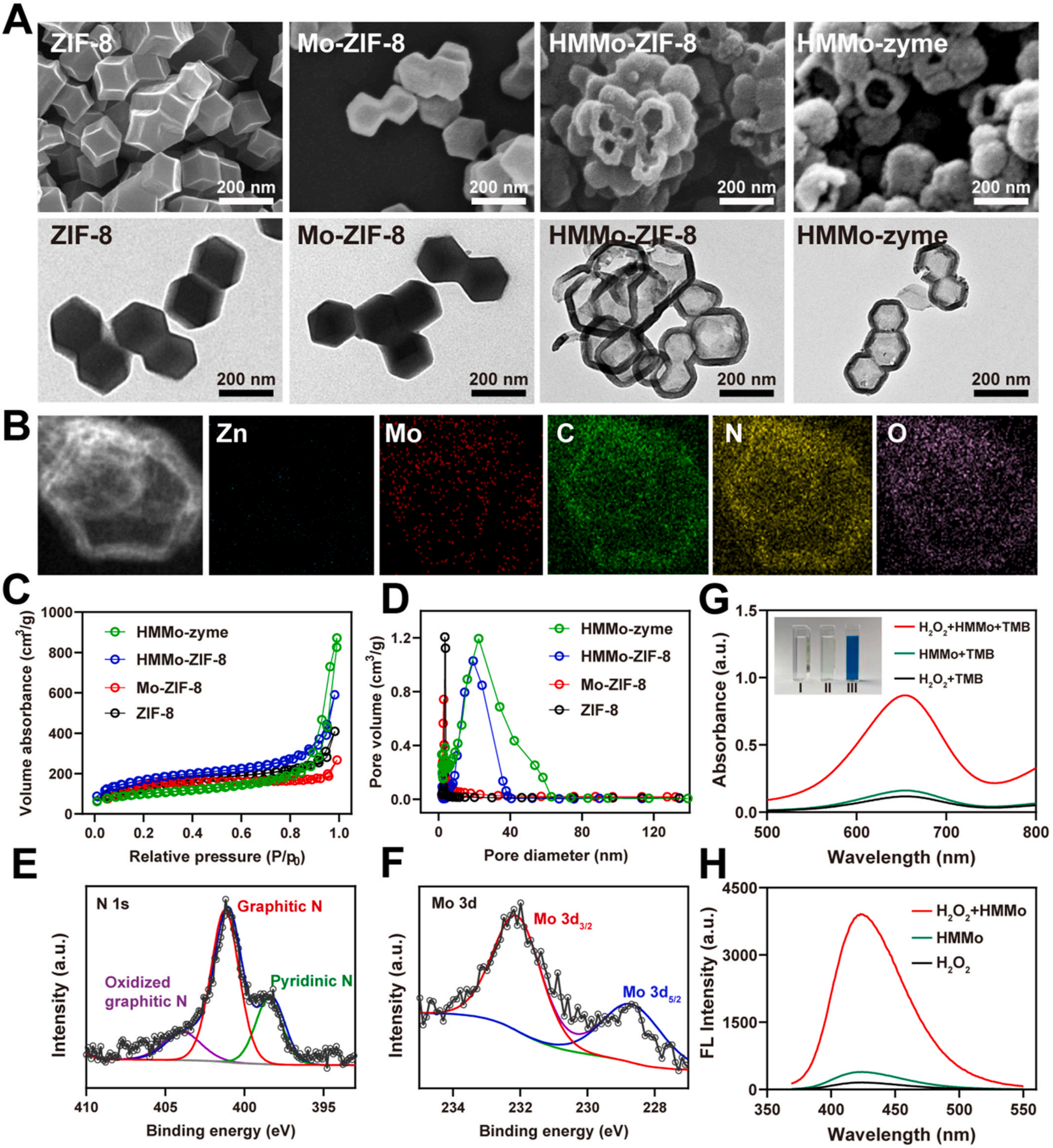

Fig. 1. (A) SEM and TEM image of ZIF-8, Mo-ZIF-8, HMMo-ZIF-8 and HMMo-zyme. (B) EDS mapping images of HMMo-zyme. (C) N_2 adsorption-desorption isotherms curve and (D) pore size distribution of ZIF-8, Mo-ZIF-8, HMMo-ZIF-8 and HMMo-zyme. High-resolution (E) N 1s and (F) Mo 3d XPS spectra of HMMo-zyme. (G) The UV spectrum of TMB treated with different groups. Inset: Photographs taken after reacting with (I) H_2O_2 + TMB, (II) HMMo-zyme + TMB, (III) H_2O_2 + HMMo-zyme + TMB. (H) The fluorescence spectrum of TA treated with different groups. Data are presented as mean ± SD.

2.7. Statistical analysis

Student t-test (two-tailed), Pearson correlation coefficient test, Wilcox test, and repeated-measures analysis of variance (ANOVA) were used for data analysis. Data were presented as mean ± SD from at least triplicate measurements. Statistical analyses were performed using SPSS 20.0 (SPSS, Chicago) or R software (https://www.r-project. org). *P < 0.05* was considered as statistically significant.

3. Results and discussion

3.1. Preparation and characterization of HMMo-zyme

Herein, a hollow mesoporous molybdenum single-atom nanozyme (HMMo-zyme) was developed using ZIF-8 as a template through an "encapsulated-pyrolysis" strategy [45,46]. During the synthesis process, $MoO_2(acac)_2$ was doped into the metal framework ZIF surface to prepare Mo-ZIF-8. Upon etching, the anionic part of tannic acid was absorbed on the surface of Mo-ZIF-8 to protect the skeleton structure from collapsing, thus obtaining the hollow structure of HMMo-ZIF-8. After pyrolysis at 900 °C, the evaporation of Zn^{2+} was accompanied by the substitution of Mo for Zn atoms in the ZIF-8 framework to form the final single-atom HMMo-zyme [47].

As shown in Fig. 1A, SEM and TEM demonstrated that the incorporation of $MoO_2(acac)_2$ as a Mo source into ZIF-8 caused negligible changes to the origin dodecahedral structure of ZIF-8 and a general particle size of ~200 nm. However, a well-defined hollow structure was obtained when Mo-ZIF-8 was etched by the following tannic acid, while the overall ZIF-8 framework still maintained intact. Interestingly, after high-temperature pyrolysis, HMMo-zyme became a smaller and more obvious hollow structure, which was attributed to structural shrinkage during pyrolysis. Furthermore, the elemental mapping showed that only a small amount of Zn retained in HMMo-zyme, while most of the C, N, O, and Mo elements were uniformly distributed within the dodecahedral framework, confirming the successful anchor of Mo atoms into the nitrogen-doped carbon matrix (Fig. 1B). The bright spots depicted in high-angle annular dark-field scanning transmission electron microscopy (HAADF-STEM) images (Fig. S1) indicated the embedding of dispersive Mo single atoms into the nitrogen-doped amorphous carbon substrate, suggesting that Mo-related SAzymes were successfully fabricated through "encapsulated-pyrolysis" strategy. The average diameter of these atomic sites was further tested to be 0.13 ± 0.03 nm, indicating that the Mo atoms were dispersed without nanoclusters/nanoparticles aggregation. The DLS results showed that the particle size of Mo-ZIF-8 slightly decreased during tannic acid corrosion, while further decreased with the subsequent pyrolysis due to a loosening of the HMMo-zyme framework (Fig. S2).

To further investigate the formation of hollow structure, BET analysis was conducted as shown in Fig. 1C. The nitrogen adsorption-desorption isotherms of ZIF-8, Mo-ZIF-8, HMMo-ZIF-8, and HMMo-zyme all exhibited typical type IV isotherm according to the IUPAC nomenclature, due to their classic mesoporous structures. The corresponding pore size distributions fitted using the BJH model were presented in Fig. 1D and Table S1, where $MoO_2(acac)_2$ absorption onto the ZIF-8 caused a decrease in both specific surface area and pore size of Mo-ZIF-8. However, tannic acid etching significantly increased the specific surface area and pore size of HMMo-ZIF-8, while the hollow structures was further amplified in HMMo-zyme after high-temperature pyrolysis, which was consistent with the results in Fig. 1A. It was notable that the surface potential of HMMo-zyme increased nearly threefold when compared to HMMo-ZIF-8 (Fig. S3), suggesting a remarkable transformation process.

The different oxidation states of metal atoms are associated with distinct macroscopic properties. Thus, XPS was utilized to further analyze the coordination environment of Mo atoms. As shown in Fig. 1E, the N1s spectra of HMMo-zyme exhibited three distinct peaks at 398, 400, and 403 eV, corresponding to the p*-transitions of pyridinic N, pyrrolic N, and graphitic N species, respectively, among which pyridinic N or pyrrolic N species have been documented to provide p-electrons to the π-conjugated structure [48]. Meanwhile, the Mo 3d spectra revealed an electronic structure capable of forming π-conjugation (Fig. 1F), indicating that nitrogen-doped carbon substrates could coordinate with Mo to form single-atom dispersed complexes after pyrolysis. Furthermore, the XRD pattern of HMMo-zyme showed no distinct crystalline features (Fig. S4), suggesting that the amorphous nature of HMMo-zyme was due to the uniform distribution of Mo atoms in single-atom form within the nanostructure.

SAzymes are ideal catalysts with HRP-like enzyme properties, which have been reported for generating toxic ·OH under the presence of H_2O_2 [33,49]. The peroxidase-like catalytic activities of the synthesized HMMo-zyme were investigated through the catalytic oxidation of TMB, one of the most widely used model substrate that would be gradually changed from colorless to blue during reaction [50,51]. The results in Fig. 1G indicated that neither H_2O_2 or HMMo-zyme alone couldn't induce any significant changes in TMB. Only when the co-existence of HMMo-zyme and H_2O_2, TMB could be oxidized into a deep blue oxTMB solution with a strong UV absorption peak at 652 nm. As a result, HMMo-zyme with the peroxidase mimicking activity can catalyze H_2O_2 to produce oxygen radicals for activating CDT. To further confirm the catalytic mechanism of HMMo-zyme on H_2O_2, TA as a typical fluorescent probe was used to detect the production of ·OH. As shown in Fig. 1H, HMMo-zyme or H_2O_2 alone couldn't induce a significant fluorescence signal change of TA. However, a distinct fluorescence signal appeared at 435 nm when both HMMo-zyme and H_2O_2 were presented, indicating that HMMo-zyme can catalyze the conversion of H_2O_2 into ·OH, which then convert TA into highly fluorescent TAOH. Furthermore, the prepared HMMO-enzyme had the best catalytic activity as the temperature reached 37 °C, thus it was especially suitable for exerting CDT effect at normal temperature *in vivo* (Fig. S5). However, HMMo-zyme showed low catalytic activity in near-neutral environments (pH = 6–7) (Fig. S6), while obtained the strongest catalytic performance in relatively acidic conditions (pH = 3), which might potentially restrict their effectiveness in bacterial microenvironments, as described above.

3.2. Photothermal-regulated GOx release from HMMo/GOx@P

To improve the catalytic efficiency of HMMo-zyme, we took advantage of the local high-glucose microenvironment in the diabetes infection model, and catalyzed the generation of gluconic acid by loading GOx to create an acidic environment, further improving the antibacterial therapeutic effect of CDT (Scheme 1). However, the hollow structure of HMMo-zyme is easy to cause the leakage of GOx in advance and conduct potential side effects to normal tissues and cells, so thermal-responsive agent PCM is further incorporated to block GOx leakage, making it release controllable through NIR in the lesion area. Considering the strong NIR absorption of graphitic carbon nitride (g-C(3)N(4)) skeleton of ZIF-8, the photothermal performance of various Mo-based SAzymes were assessed by measuring laser irradiation-induced temperature changes. As presented in Fig. 2A, HMMo-ZIF-8 exhibited slightly superior photothermal responsiveness than that of Mo-ZIF-8. However, the pyrolyzed HMMo-zyme showed further amplified photothermal behavior, possibly due to the burned ZIF-8 frame, and the remaining black amorphous carbon carrier could improve the photothermal conversion efficiency more effectively [52,53]. Thermographic images further revealed a similar rising trend and high photothermal conversion capability of HMMo-zyme, which was crucial for further manipulating GOx release (Fig. 2B). The concentration-dependent and power-density-dependent temperature increases caused by NIR irradiation were completely reversible upon cessation of irradiation (Figs. S7 and S8). To assess photothermal conversion efficiency of HMMo-zyme, fitting curves of the negative logarithm of the temperature difference versus time were calculated in Fig. 2C–Fig. S9 and S10, where

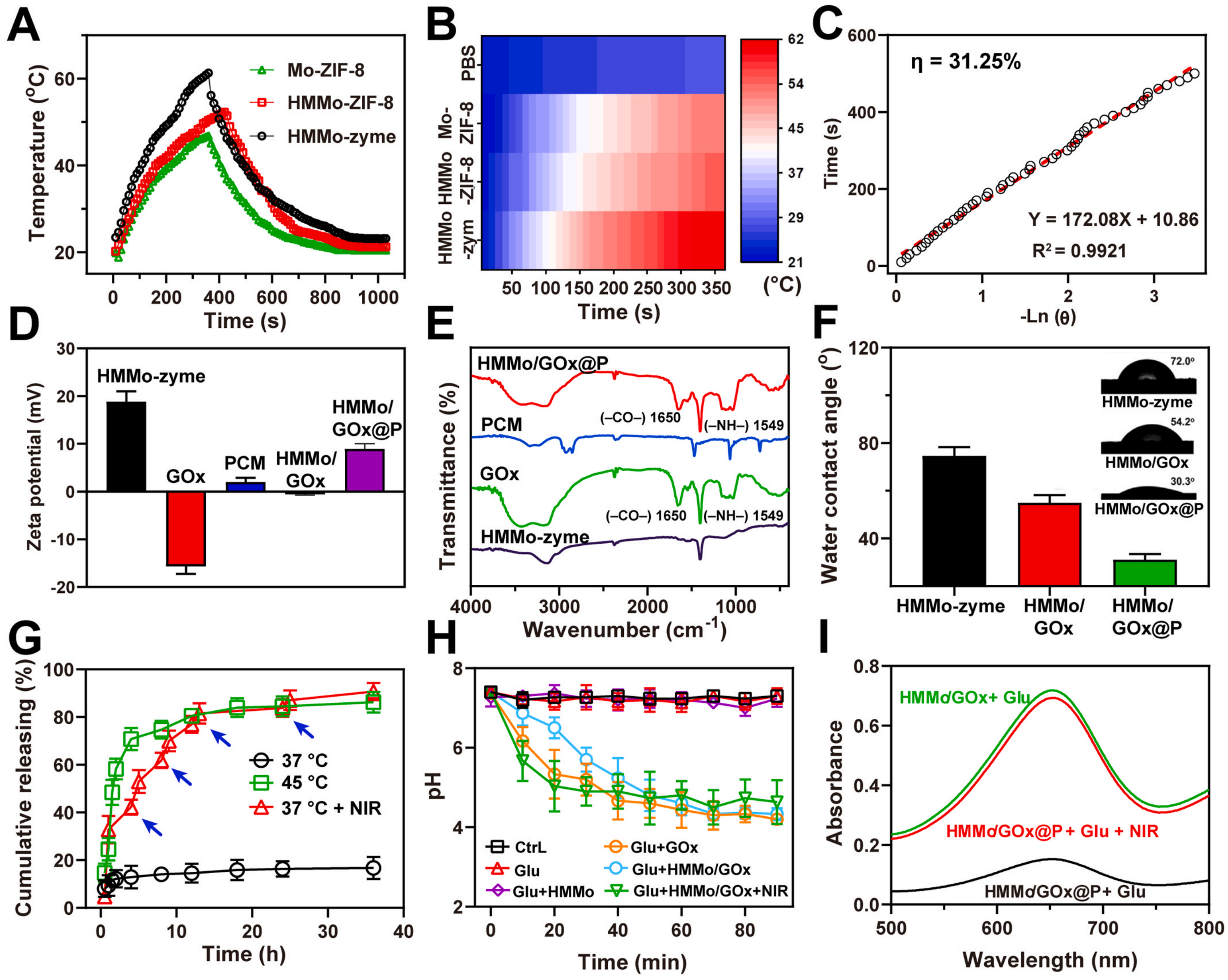

Fig. 2. (A) Temperature profile of Mo-ZIF-8, HMMo-ZIF-8, and HMMo-zyme (100 μg/mL) under photothermal heating and natural cooling. (B) The corresponding temperature mapping images of Mo-ZIF-8, HMMo-ZIF-8, and HMMo-zyme at 808 nm laser irradiation with a power density of 1.5 W/cm^2 for 6 min. (C) Photothermal transduction efficiency (η) of the HMMo-zyme. (D) Zeta potential, (E) FTIR spectrum and (F) water contact angle image of HMMo-zyme before and after PCM/GOx encapsulation. (G) Kinetic release profiles of GOx from HMMo/GOx@P at different incubation temperatures or upon NIR irradiation. The blue arrows indicated the laser is on. (H) pH monitoring in different treated groups. (I) UV–vis spectra of HMMo/GOx + Glu, HMMo/GOx@P + Glu with or without NIR irradiation (1.5 W/cm^2).Data are presented as mean ± SD. (For interpretation of the references to color in this figure legend, the reader is referred to the Web version of this article.)

HMMo-zyme was ascertained to be 31.25 % ± 1.74 %, which was significantly higher than Mo-ZIF-8 (23.62 % ± 2.20 %) and HMMo-ZIF-8 (28.15 % ± 1.23 %). Moreover, HMMo-zyme showed almost similar photothermal behaviors after five consecutive heating and cooling cycles, revealing that the as-obtained HMMo-zyme possessed satisfactory photothermal stability (Fig. S11). These prominent photothermal performances highlight the possibilities of HMMo-zyme to be served as photothermal inducer to trigger the phase transition of PCM for GOx tuneable release.

Furthermore, the hollow structure of HMMo-zyme with abundant pore size and volume was suitable for GOx and PCM encapsulation. It was obvious that Zeta potential of HMMo/GOx decreased significantly due to the loading of negatively charged of GOx, which then increased after the effective loading of PCM (Fig. 2D). These changes of Zeta potential predicted the successful synthesis of HMMo/GOx@P. Moreover, the FTIR spectra of PCM, GOx, HMMo-zyme, and HMMo/GOx@P were presented in Fig. 2E, where the characteristic peaks at ~1650 cm^{-1} and ~1549 cm^{-1} corresponded to amide I (–CO– and –CN– stretching) and amide II (–NH– bending) in GOx, while the broad peak at 2850–2950 cm^{-1} was attributed to methylene groups in PCM. Additionally, the surface of PCM contains abundant non-polar hydroxyl groups, indicating their potential strong binding affinity with water molecules. As shown in Fig. 2F, the water contact angle of HMMo/GOx@P was significantly reduced when compared to bare HMMo-zyme, confirming the successful embedding of PCM into HMMo-zyme. Further, according to the established GOx standard curve (Fig. S12), the encapsulation ratio and drug loading capacity of GOx in HMMo/GOx@P were determined to be 78.62 % and 10.25 %, respectively, which might be attributed to the hollow/mesoporous structure of HMMo-zyme, PCM crosslinking, and/or hydrophobic-hydrophobic interactions.

To verify the PCM-manipulated GOx release, the release efficiency of GOx in different scenarios was monitored (Fig. 2G). In the ordinary 37 °C environment, the cumulative release of GOx from HMMo/GOx@P was approximately 16.73 ± 4.62 % over 24 h due to the conjugation of PCM. However, since high temperature (45 °C) could induce the phase transition of PCM, GOx showed more rapid release within 4 h, and reached to equilibrium at 8 h with a cumulative release of 74.69 ± 3.71 %. At 24 h, the amount of release was 84.54 ± 4.17 %, which supported that high temperature could effectively promote GOx release for further cascade catalytic reaction. Taking advantage of the high photothermal conversion efficiency of HMMo-zyme, GOx was continuously released after short laser irradiation (1.5 W/cm^2, 30s) at different periods of time. The rate of GOx release reached to 86.72 ± 3.18 % after 24 h, similar to the results obtained by high temperature incubation. Therefore, the local high temperature formed by laser irradiation can induce PCM phase transition and realize the pulse administration of GOx *in vitro* and *in vivo*.

As mentioned above, the released GOx can continuously catalyze Glu to produce acidic substances (gluconic acid) and H_2O_2, which can further act as substrates catalyzed by HMMo-zyme to produce bactericidal •OH mediated CDT strategy. Although GOx can be released controllably at the site of diabetic infected wounds, its ability to catalyze Glu to gluconic acid and H_2O_2 still needs to be further verified. Therefore, the activation of HMMo/GOx was then monitored in PBS buffer (pH 8.0) to simulate the physiological microenvironment of diabetic wounds. The result in Fig. 2H showed that HMMo/GOx significantly reduced the pH value of the solution in the present of Glu, achieving an effect similar to that of pure GOx at the same concentration. The pH value further decreased with the increase of Glu dosage, which was conducive to improve the catalytic efficiency of HMO-enzyme (Fig. S13). It is worth noting that NIR irradiation can induce PCM phase transition and promote the rapid release of GOx for Glu catalysis, resulting in a rapid decline in pH in the early stage. However, the release rate of GOx slowed down over time, and the change of pH reached to equilibrium, thus further confirming the effects of NIR excitation on pH reduction. Simultaneously, the formation of H_2O_2 was detected by TMB as an indicator, which could be tuned by H_2O_2 to blue color with a characteristic UV absorption at 652 nm. However, the pure GOx did not cause a significant change in the absorption of TMB due to the lack of HMMO-enzyme, and HMMO-enzyme itself also could not perform peroxidase-like activity without H_2O_2 assistance. Only when HMMo/GOx catalyzed Glu to produce H_2O_2, TMB could be catalyzed by HMMO-enzyme with strong UV absorption at 652 nm (Fig. S14), indicating that the cascade catalytic process was successfully completed.

Furthermore, we also validated the strategies for NIR-mediated HMMo/GOx@P to trigger GOx release and modulate catalysis precisely. Fig. 2I showed that the UV absorption of TMB was significantly increased after the reaction of HMMo/GOx with Glu, where GOx catalyzed Glu to produce acidic substances and H_2O_2 for further induction of the cascade CDT strategy. However, PCM blocked the release of GOx from HMMo/GOx@P, resulting in the restriction of subsequent catalytic reactions. Under NIR irradiation, high temperature induced PCM phase transition to initiate the GOx release for Glu catalysis, and subsequent generation of ·OH facilitated by HMMo-zyme catalytic activity. The significant absorption peak appeared at 652 nm strongly confirmed that the cascade catalytic reaction was successfully excited and precisely controlled by the NIR. Together, the changes of pH and TMB model demonstrated the availability of NIR-triggered strategy, which was expected to mediate CDT sterilization against diabetic infections/wounds healing.

3.3. Antibacterial ability and biosafety of HMMo/GOx@P

Herein, NIR triggered the response of HMMo/GOx@P to release GOx, which subsequently catalyzed Glu to produce H_2O_2 and gluconic acid, tuning the local pH down for HMMO-Zyme mediated cascade CDT toward bacteria. However, hyperthermia mediated by NIR will not only kill the target bacteria, but also burn the normal cells during the treatment. Therefore, to minimize the side effects of hyperthermia and to maximize the CDT effect on bacteria, we explored the optimal HMMo/GOx@P-induced photothermal effect to ensure PCM phase transition without compromising the normal cell viability. The results indicated that HMMo/GOx@P did not cause significant cytotoxicity in the absence of NIR, even at the highest concentration, confirming the safety and biocompatibility of HMMo/GOx@P (Fig. S15). However, when the concentration of HMMo/GOx@P exceeded 100 μg/mL, the NIR-induced photothermal effect resulted in significant toxicity to both HUVEC and NRK cells. Therefore, 100 μg/mL of HMMo/GOx@P was used for further study, at which the PCM phase transition can be induced to promote more than 80 % GOx release (Fig. 2G) without cytotoxicity.

Furthermore, the antibacterial efficacy of CDT mediated by ·OH was studied by using *E. coli* and *S. aureus* as representative Gram-positive and Gram-negative model strain. Bacteria in the logarithmic growth phase were treated with different strategies: (I) PBS (control), (II) HMMo-zyme, (III) HMMo-zyme + NIR, (IV) HMMo/GOx@P + Glu, (V) HMMo/GOx + Glu, and (VI) HMMo/GOx@P + Glu + NIR (1.5 W/cm^2 5 min). For agar plate counting test (Fig. 3A), the HMMo-zyme and HMMo-zyme + NIR groups have negligible bactericidal effects, exhibiting similar bacterial survival rate with the control group. It was worth noting that the photothermal conversion efficiency of HMMo-zyme was not enough to induce PTT for bacterial damage, so NIR only acted as a switch to induce the depolymerization of PCM for the cascade release of GOx. The number of *E. coli* and *S. aureus* treated with HMMo/GOx@P + Glu decreased to 80.36 % and 79.47 % respectively (Fig. 3B and C), possibly due to the blockage of PCM to limit H_2O_2 generation with restricted CDT effects on bacteria. Furthermore, the antibacterial effect of HMMo/GOx + Glu was increased due to most of GOx released gradually without PCM constraint, resulting in enhanced CDT effects. Upon NIR irradiation, HMMo/GOx@P + Glu treatment exhibited superior antibacterial performance, where the survival rates of *E. coli* and *S. aureus* reduced to 23.33 % and 17.06 %, respectively. This bactericidal efficacy was attributed to NIR-accelerated GOx release to facilitate the conversion of Glu to H_2O_2, which was further catalyzed into ·OH by HMMo-zyme to extend bacterial elimination.

To further visualize the antibacterial performance of HMMo/GOx@P, *in vitro* antibacterial activity was also assessed using a Live/Dead two-color kit (Fig. 3D). When treated with HMMo-zyme, all of bacteria survived (green spots) in spite of with or without NIR irradiation, while treatment with HMMo/GOx@P + Glu caused a certain number of bacteria damage (a clearer merged image with red or yellow dots for a more accurate description of dead bacteria) due to the production of ·OH. It was notable that although a large amount of GOx was blocked by PCM, some GOx still leaked to trigger a cascade catalytic reaction. Importantly, the proportion of dead bacteria (red or yellow) were significantly increased under NIR irradiation, showing the notable inhibition effects against *E. coli* and *S. aureus*, which was consistent with the results of plate counting.

SEM was conducted to observe the morphological changes of *E. coli* and *S. aureus* after different treatments. As shown in Fig. 3E, HMMo-zyme and HMMo-zyme + NIR groups showed intact morphology and smooth surfaces of bacteria as similar as control group, while certain degree of damage in the bacteria took place after incubation with HMMo/GOx + Glu. Bacteria were collapsed and deformed obviously under NIR irradiation, as the efficient photothermal responsiveness of HMMo-zyme generated hyperthermia to accelerate release of GOx for improving CDT effect. Together, these results demonstrated that NIR controllably activated HMMo/GOx@P to release GOx, which then catalyzed the production of toxic ·OH through the cascade triggering strategy, resulting in severe oxidative damage toward *E. coli* and *S. aureus*.

For further *in vivo* application, the biocompatibility and biosafety of the SAzymes were determined through cytotoxicity and hemolysis assay. The HMMo-zyme and HMMo/GOx@P (100 μg/mL) were not cytotoxic to NRK and HUVEC, with viability over 95 % (Fig. 4A), highlighting their robust safety profile. Additionally, the hemolysis rates of HMMO-enzyme and HMMo/GOx@P were lower than 3 %, and the hemolysis phenomenon was negligible when compared with positive control group (H_2O), as depicted in Fig. 4B. The hemolysis rate remained at a low level even after incubation for more than 24 h, enabling it could meet the safety standard for *in vivo* application (Fig. 4C).

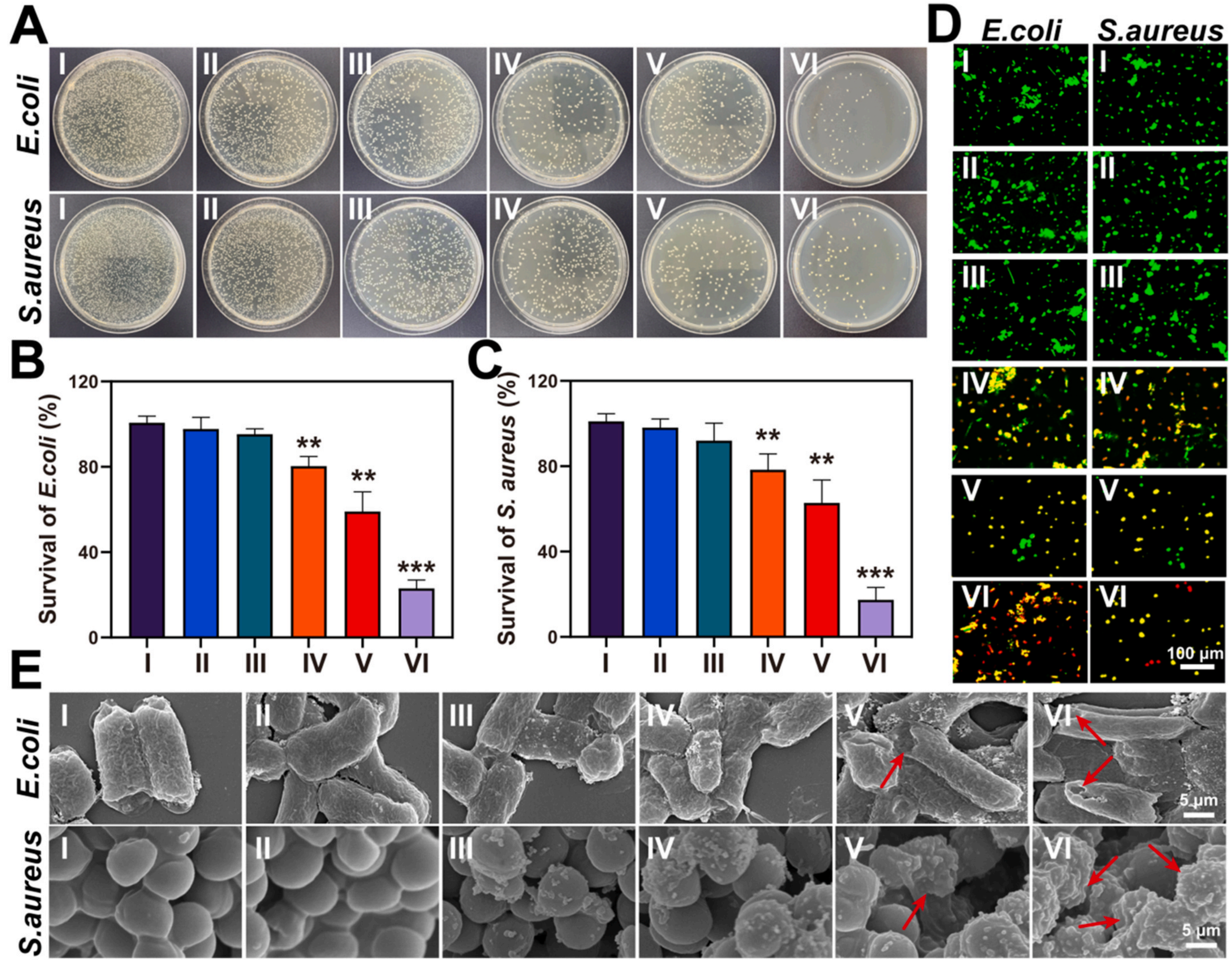

Fig. 3. (A) Digital photographs of remaining bacteria-inoculated agar plates by *E. coli* and *S. aureus* treated with different groups. Survival rates of (B) *E. coli* and (C) *S. aureus* with different treatment. (D) CLSM images for live/dead bacterial staining assay of *E. coli* and *S. aureus* after treatment of respective groups. (E) SEM images of *E. coli* and *S. aureus* treated with different groups. The red arrows represent the distinct signs of bacterial deformation. The treated groups included (I) PBS (control), (II) HMMo-zyme, (III) HMMo-zyme + NIR, (IV) HMMo/GOx@P + Glu, (V) HMMo/GOx + Glu, and (VI) HMMo/GOx@P + Glu + NIR (1.5 W/cm^2 5 min). Data are presented as mean ± SD. $^*p < 0.05$, $^{**}p < 0.01$ and $^{***}p < 0.001$. (For interpretation of the references to color in this figure legend, the reader is referred to the Web version of this article.)

Subsequently, *in vivo* toxicity of HMMo-zyme and HMMo/GOx@P against the major organs was also analyzed by H&E staining and biochemical assays (the hepatic function (i.e. aspartate aminotransferase-AST, alanine aminotransferase-ALT, and alkaline phosphatase-ALP), and kidney function (i.e. UREA, creatinine-CRE and Uric Acid-UA) [54]. As shown in Fig. 4D–H&E staining showed no significant histopathological damage, and there was no apparent difference between the treated group and the control group. Inflammatory response was negligible in the lungs and liver of the mice. Additionally, the proportion of red pulp to white pulp in the spleen, as well as the number and volume of glomeruli and renal tubules remained normal. No structural abnormalities were found in the myocardium. The ALT/AST/CRE/UREA/UA levels of the treated group were comparable to the control group, which further indicated HMMo/GOx@P-mediated CDT had acceptable biosafety and biocompatibility (Fig. 4E). Observations of vital signs over 7 days post-treatment in mice showed no significant impact on mice growth (Fig. 4F–H), which revealed the negligible side-effects of HMMo-zyme and HMMo/GOx@P *in vivo*. Together, these results all manifested the admirable biocompatibility and biosafety of HMMo-zyme and HMMo/GOx@P, holding their great promise for further *in vivo* applications.

3.4. Antibacterial activity of HMMo/GOx@P in vivo

The healing process of diabetic wound is mainly interfered by bacterial infection, which delays the transition of healing procedure from inflammation to proliferative phase [55,56]. Herein, HMMo/GOx@P were designed to suppress bacteria and regulate immune responses, thereby accelerating diabetic would healing. Firstly, a diabetic infected model was established by injecting STZ and dropping *S. aureus* in the skin wounds of mice [27]. Afterwards, the wounds were treated with HMMo-zyme, HMMo-zyme + NIR, HMMo/GOx, HMMo/GOx@P, and HMMo/GOx@P + NIR, and the wounds without any treatment were set as control group. The statistical analysis of wound area was analyzed every two days by specialized image processing software such as Image J and Image-Pro Plus. As exhibited in Fig. 5A, the wounds in control group, HMMo-zyme group, and HMMo-zyme + NIR group showed obvious abscess on the 3rd day, suggesting the serious wound infection in the mice model. However, there was no obvious wound infection in HMMo/GOx, and HMMo/GOx@P group, owing to the superior

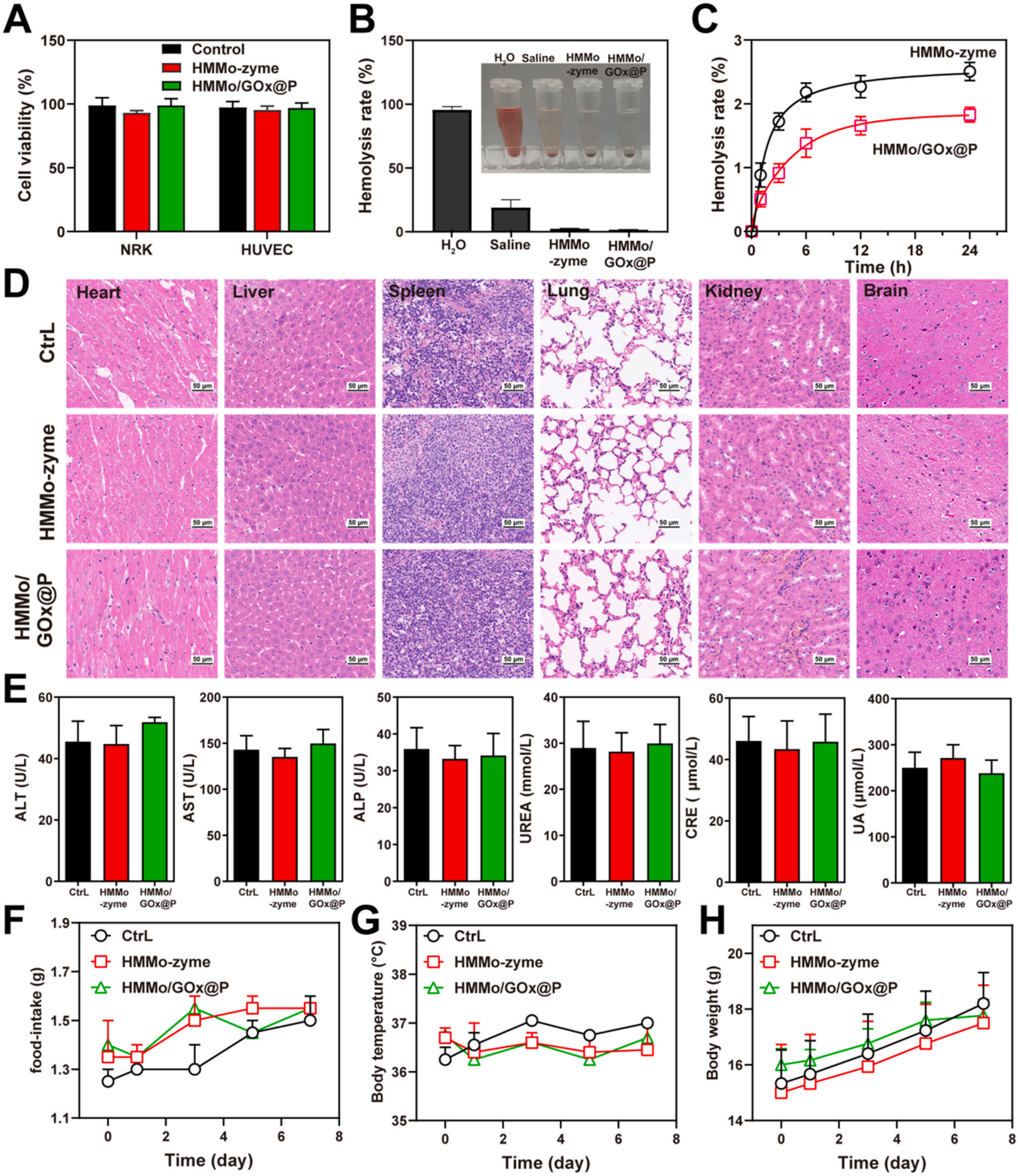

Fig. 4. (A) Cytotoxicity of NRK and HUCEV cells following treatment with HMMo-zyme and HMMo/GOx@P (100 μg/mL). (B) Hemolysis test of HMMo-zyme and HMMo/GOx@P with the positive control of H_2O. (C) Relative hemolysis ratio of HMMo-zyme and HMMo/GOx@P with 24 h. (D) H&E staining of major organs following indicated treatment in mice. (E) Blood biochemistry analysis of liver/kidney function markers ALT, AST, ALP and UREA, CRE and UA following indicated treatment combinations in mice. (F) Body weight, (G) body temperature and (H) food-intake of mice with different treatment in 7 days, respectively. Data are presented as mean ± SD.

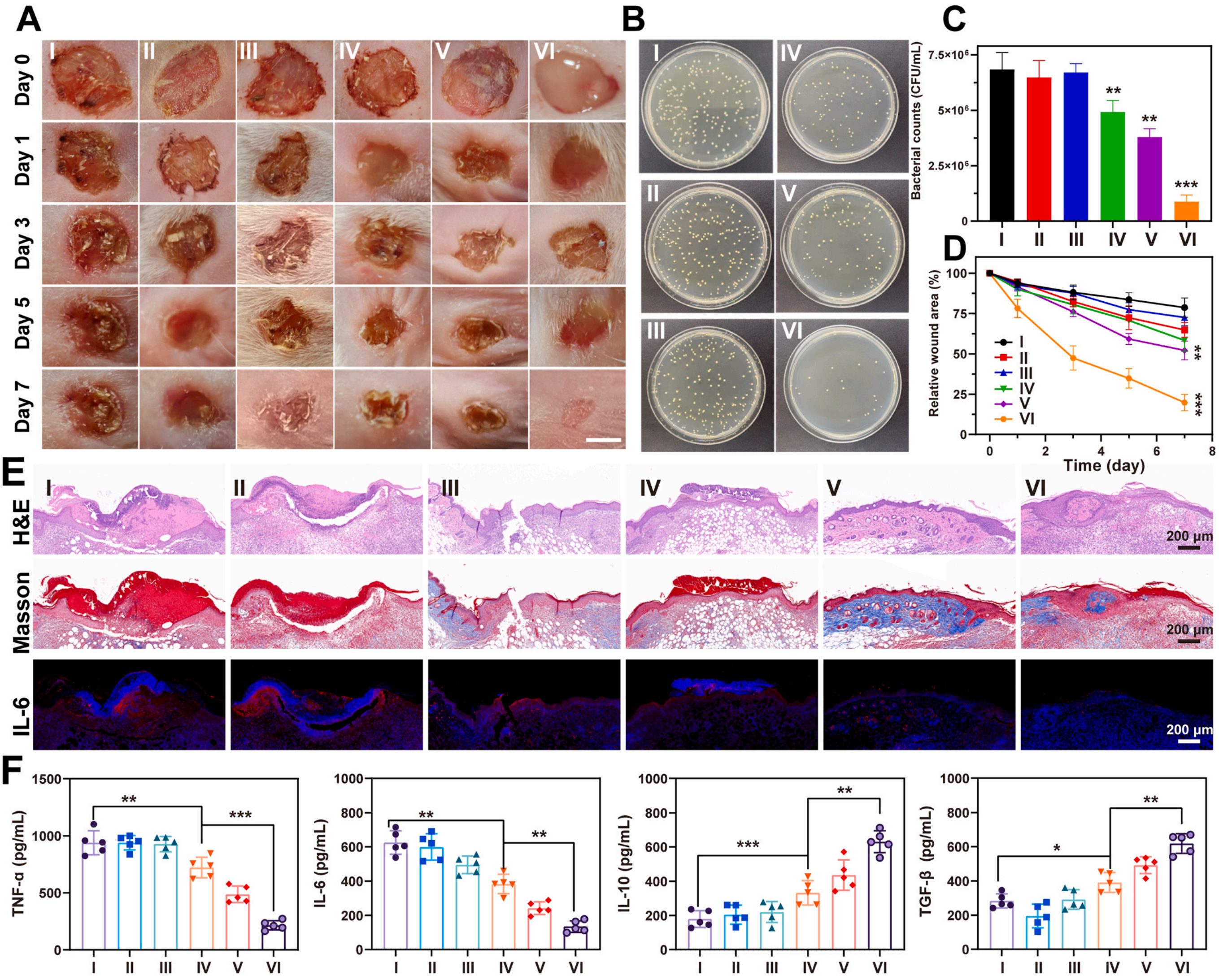

Fig. 5. (A) Digital photo of *S. aureus*-infected wounds after treatment for 7 days by different groups, and the scale bar is 3 mm. These wounds were observed every 2 days, the PBS-treated mice were set as the control group. (B) Photographs of bacterial colonies obtained from *S. aureus*-infected wounds treated by different groups and (C) Quantitative statistics of the number of bacterial colonies through standard plate counting assay. (D) The wounds residual area after treatment for 7 days by different groups. (E) H&E, Masson and IL-6 staining images of wound tissue slices after treatment for 7 days by different groups. (F) TNF-α, IL-6, Il-10, and TGF-β levels of infected mice after treatment for 7 days by different groups. The treated groups included (I) PBS, (II) HMMo-zyme, (III) HMMo-zyme + NIR, (IV) HMMo/GOx@P, (V) HMMo/GOx, and (VI) HMMo/GOx@P + NIR (1.5 W/cm^2 5 min). Data are presented as mean ± SD. $^*p < 0.05$, $^{**}p < 0.01$ and $^{***}p < 0.001$.

antibacterial properties of H_2O_2 or ·OH produced by Glu responsive regulations. It was note that the wounds had a significant shrinkage after HMMo/GOx@P + NIR treatment. On day 7, the wound areas in all groups showed an evident wound closure, among which the size of wound in HMMo/GOx@P + NIR group was much smaller (approximately 21 %) than other groups, while control group showed the largest size of wound (approximately 80 %) (Fig. 5D). Therefore, it was concluded that HMMo/GOx@P with NIR irradiation intensified GOx release and the subsequent cascade catalytic reaction for producing ·OH, which significantly inhibited wound infection and accelerated wound closure.

Moreover, wound tissues were collected and homogenized for bacterial culture. As shown in Fig. 5B, a remarkable reduction of bacterial amounts was observed in the HMMo/GOx@P + NIR group, further indicating the prominent antibacterial performance. The quantitative results analyzed by colony counting revealed that although other treatments demonstrated certain bacteriostatic effect, HMMo/GOx@P + NIR treatment showed more pronounced bacterial inhibition (Fig. 5C), which was attributed to the catalytic conversion of H_2O_2 into the more potent ·OH for bacterial eradication. Thus, this strategy integrating NIR-switched release, cascade amplified catalysis and Fenton-like reactions demonstrated effective and promising potentials for diabetic infected wound healing.

To further assess the therapeutic efficacy of NIR-mediated HMMo/GOx@P on infected mice wounds, histological staining was performed on the wounds of the different groups (Fig. 5E). The H&E staining results found that after HMMo/GOx@P + NIR treatment, a new epidermal layer appeared in the injured area, and the residual connective tissue could be seen on the top of dermis. HMMo/GOx@P + NIR achieved satisfactory healing effects in diabetic wound repairs, where the wound area, new epidermal thickness and lesion thickness were notably higher than those of other groups. Additionally, Masson staining analysis found fewer collagen fibers in the wounds of control group, while HMMo/GOx@P + NIR group showed highest amounts of collagen, which was consistent with the results of H&E staining. The enhanced collagen deposition can improve skin strength, accelerate healing, and shrink scarring, thus further indicating the therapeutic effects of HMMo/GOx@P + NIR treatment. Furthermore, immunofluorescence staining showed the decreased IL-6 expression in HMMo/GOx@P + NIR treated group, suggesting the alleviated inflammation contributed to the facilitated healing. These results suggested that NIR-mediated GOx release and cascade CDT could effectively inhibit/kill bacteria, regulate inflammation and facilitate the process of wound repair.

To further evaluate the inflammation regulation capabilities of HMMo/GOx@P in wound healing, the expression levels of pro-inflammatory cytokines (tumor necrosis factor-alpha (TNF-α) and IL-6) and anti-inflammatory cytokines (interleukin-10, IL-10, and transforming growth factor-beta, TGF-β) were tested by using ELISA following different treatments. As shown in Fig. 5F, the results demonstrated that in the absence of NIR irradiation, GOx hindered the production of H_2O_2 or toxic·OH, leading to the elevated levels of pro-inflammatory cytokines. In contrast, the HMMo/GOx group was capable of generating H_2O_2 and showed a reduction in TNF-α and IL-6 levels due to partial bacterial elimination. Notably, levels of these proinflammatory cytokines were further down-regulated in the NIR-irradiated HMMo/GOx@P group. Meanwhile, the anti-inflammatory cytokine levels displayed opposite trend, which were increased as the bacteria were eradicated. These results suggested that NIR-mediated HMMo/GOx@P effectively regulated the inflammatory responses of wound tissue, thereby promoting faster wound healings. Based on these inflammation regulation, collagen deposition and bacterial elimination effects, the developed NIR-mediated HMMo/GOx@P provides a novel strategy for the healing and treatment of diabetic infections/wounds.

4. Conclusion

In summary, this study successfully developed HMMo-zyme with a well-defined hollow and mesoporous structure using ZIF-8 as a template, where the favorable pore size parameters and photothermal conversion efficiency can achieve GOx encapsulation and NIR-responsive cascade CDT toward diabetic infections/wounds. Considering the alkaline microenvironment and the high concentration of Glu in diabetic wounds, the GOx trapped in PCM could be triggered to release via NIR, which therefore dropped the local pH and supplemented H_2O_2, broke the pH and H_2O_2 limitations to maximize the peroxidase-like activity of HMMo-zyme for CDT sterilization. *In vivo* studies further verified that HMMo/GOX@P-mediated CDT could facilitate diabetic wound healings by inhibiting wound infections, modulating inflammation factors, accelerating the deposition of collagens at wound site. Therefore, taking advantages of NIR switching, pH tuning and enhanced antibacterial effects, this study offers a new approach for the treatment of diabetic infection/wound under the physiological conditions. More importantly, this cascade catalysis strategy of HMMo-zyme can break the physiological limitations of diabetic wounds, which might be easily extended to other SAzymes, making it suitable for the treatment of various bacterial infectious diseases.

CRediT authorship contribution statement

Jingwei Wang: Writing – original draft, Conceptualization. **Yin Yu:** Formal analysis, Data curation, Conceptualization. **Lingzhi Chen:** Methodology, Investigation, Formal analysis. **Jiaqi Yu:** Methodology, Investigation. **Xiaoying Jin:** Methodology, Investigation. **Runmin Zeng:** Methodology, Investigation. **Xiaomin Luo:** Formal analysis, Conceptualization. **Yanguang Cong:** Supervision, Software, Resources. **Guangxian Xu:** Software, Resources, Methodology. **Jianglin Zhang:** Supervision, Project administration. **Xueqin Huang:** Writing – review & editing, Funding acquisition, Data curation. **Jiang Pi:** Writing – review & editing, Supervision, Project administration.

Declaration of competing interest

The authors declare no competing financial interest.

Acknowledgements

This work is financially supported by the National Natural Science Foundation of China (82304438), Guangdong Basic and Applied Basic Research Foundation (2022A1515110618), construction project of Nano Technology and Application Engineering Research Center of Guangdong Medical University (4SG24179G), Foundation of State Key Laboratory of Pathogenesis, Prevention and Treatment of High Incidence Diseases in Central Asia (SKL-HIDCA-2024-GD11), Medical-Industrial Integration Project of Songshan Lake (4SG22309P), Discipline Construction Project of Guangdong Medical University (4SG24010G). We are very thankful to Dr Xiang Yu, from the Analytical and Testing Center Jinan University for providing the TEM and EDS technical support to carry out this research.

Appendix A. Supplementary data

Supplementary data to this article can be found online at https://doi.org/10.1016/j.mtbio.2025.101557.

Data availability

Data will be made available on request.

References

[1] M.G. Yu, D. Gordin, J. Fu, K. Park, Q. Li, G.L. King, Protective factors and the pathogenesis of complications in diabetes, Endocr. Rev. 45 (2024) 227–252, https://doi.org/10.1210/endrev/bnad030.

[2] Y. Liu, S. Zeng, W. Ji, H. Yao, L. Lin, H. Cui, H.A. Santos, G. Pan, Emerging theranostic nanomaterials in diabetes and its complications, Adv. Sci. 9 (2022) 2102466, https://doi.org/10.1002/advs.202102466.

[3] Z. Hu, J. Shan, X. Jin, W. Sun, L. Cheng, X.-L. Chen, X. Wang, Nanoarchitectonics of *in situ* antibiotic-releasing acicular nanozymes for targeting and inducing cuproptosis-like death to eliminate drug-resistant bacteria, ACS Nano 18 (2024) 24327–24349, https://doi.org/10.1021/acsnano.4c06565.

[4] W. Wang, Y. Cui, X. Wei, Y. Zang, X. Chen, L. Cheng, X. Wang, $CuCo_2$ O_4 nanoflowers with multiple enzyme activities for treating bacterium-infected wounds via cuproptosis-like death, ACS Nano 18 (2024) 15845–15863, https://doi.org/10.1021/acsnano.4c02825.

[5] W. Zhang, Y. Lv, Q. Niu, C. Zhu, H. Zhang, K. Fan, X. Wang, Zinc oxide-enhanced copper sulfide nanozymes promote the healing of infected wounds by activating immune and inflammatory responses, Small (2024) 2406356, https://doi.org/10.1002/smll.202406356.

[6] Y. Sun, W. Zhang, Z. Luo, C. Zhu, Y. Zhang, Z. Shu, C. Shen, X. Yao, Y. Wang, X. Wang, ZnO-CuS/F127 hydrogels with multienzyme properties for implant-related infection therapy by inhibiting bacterial arginine biosynthesis and promoting tissue repair, Adv Funct Materials (2024) 2415778, https://doi.org/10.1002/adfm.202415778.

[7] A.C. Fenneman, M. Weidner, L.A. Chen, M. Nieuwdorp, M.J. Blaser, Antibiotics in the pathogenesis of diabetes and inflammatory diseases of the gastrointestinal tract, Nat. Rev. Gastroenterol. Hepatol. 20 (2023) 81–100, https://doi.org/10.1038/s41575-022-00685-9.

[8] J. Yuan, Y.J. Hu, J. Zheng, J.H. Kim, T. Sumerlin, Y. Chen, Y. He, C. Zhang, J. Tang, Y. Pan, M. Moore, Long-term use of antibiotics and risk of type 2 diabetes in women: a prospective cohort study, Int. J. Epidemiol. 49 (2020) 1572–1581, https://doi.org/10.1093/ije/dyaa122.

[9] X. Huang, L. Chen, Y. Lin, K.I. Tou, H. Cai, H. Jin, W. Lin, J. Zhang, J. Cai, H. Zhou, J. Pi, Tumor targeting and penetrating biomimetic mesoporous polydopamine nanoparticles facilitate photothermal killing and autophagy blocking for synergistic tumor ablation, Acta Biomater. 136 (2021) 456–472, https://doi.org/10.1016/j.actbio.2021.09.030.

[10] X. Huang, H. Cai, H. Zhou, T. Li, H. Jin, ColinE. Evans, J. Cai, J. Pi, Cobalt oxide nanoparticle-synergized protein degradation and phototherapy for enhanced anticancer therapeutics, Acta Biomater. 121 (2021) 605–620, https://doi.org/10.1016/j.actbio.2020.11.036.

[11] X. Huang, L. Chen, Y. Zhang, S. Zhou, H.-H. Cai, T. Li, H. Jin, J. Cai, H. Zhou, J. Pi, GE11 peptide conjugated liposomes for EGFR-targeted and chemophotothermal combined anticancer therapy, Bioinorgan. Chem. Appl. 2021 (2021) 1–15, https://doi.org/10.1155/2021/5534870.

[12] Y. Ma, S. Li, X. Lin, Y. Chen, A perspective of lipid nanoparticles for RNA delivery, Explorations 4 (2024) 20230147, https://doi.org/10.1002/EXP.20230147.

[13] T. Feng, W. Ahmed, T. Ahmed, L. Chen, Nanoparticles derived from herbal preparations May represent a novel nucleic acid therapy, Interdisciplinary Medicine 2 (2024) e20230029, https://doi.org/10.1002/INMD.20230029.

[14] J.M.V. Makabenta, A. Nabawy, C.-H. Li, S. Schmidt-Malan, R. Patel, V.M. Rotello, Nanomaterial-based therapeutics for antibiotic-resistant bacterial infections, Nat. Rev. Microbiol. 19 (2021) 23–36, https://doi.org/10.1038/s41579-020-0420-1.

[15] W. Huang, L. Meng, Y. Chen, Z. Dong, Q. Peng, Bacterial outer membrane vesicles as potential biological nanomaterials for antibacterial therapy, Acta Biomater. 140 (2022) 102–115, https://doi.org/10.1016/j.actbio.2021.12.005.

[16] Y. Luo, X. Jia, X. Wu, L. Diao, Y. Zhao, X. Liu, Y. Peng, W. Zhong, M. Xing, G. Lyu, Bacteria-activated macrophage membrane coated ROS-responsive nanoparticle for targeted delivery of antibiotics to infected wounds, J. Nanobiotechnol. 22 (2024) 781, https://doi.org/10.1186/s12951-024-03056-5.

[17] C. Zhang, Y. Zuo, T. Zhang, X. Zhang, J. Ling, C. Liu, H. Chen, X. Zhou, M. Wang, Y. Deng, Y. Liu, J. Lu, Advances in nanoscale carrier-based approaches to reduce toxicity and enhance efficacy of podophyllotoxin, Acta Materia Medica 2 (2023), https://doi.org/10.15212/AMM-2023-0038.

[18] J. Xia, C. Hu, Y. Ji, M. Wang, Y. Jin, L. Ye, D. Xie, S. Jiang, R. Li, Z. Hu, J. Dai, Copper-loaded nanoheterojunction enables superb orthotopic osteosarcoma therapy via oxidative stress and cell cuproptosis, ACS Nano 17 (2023) 21134–21152, https://doi.org/10.1021/acsnano.3c04903.

[19] Y. Lin, X. Huang, L. Hu, H. Zhou, A. Yang, J. Xu, W. Chen, X. Zeng, P. Sun, X. Zhong, H. Zhou, H. Cai, Self-assembly MoS2@MnO2 nanoflowers for the fluorescence/magnetic resonance dual-modal sensing of H2O2 and photothermal therapy, ACS Appl. Nano Mater. 6 (2023) 22265–22274, https://doi.org/10.1021/acsanm.3c04392.

[20] J. Xin, Z. Yang, S. Zhang, L. Sun, X. Wang, Y. Tang, Y. Xiao, H. Huang, W. Li, Fast fabrication of "all-in-one" injectable hydrogels as antibiotic alternatives for enhanced bacterial inhibition and accelerating wound healing, J. Nanobiotechnol. 22 (2024) 439, https://doi.org/10.1186/s12951-024-02657-4.

[21] X. Lu, W. Deng, S. Wang, S. Zhao, B. Zhu, B. Bai, Y. Mao, J. Lin, Y. Yi, Z. Xie, X. Wang, Y. Lu, X. Huang, T. You, X. Chen, W. Sun, X. Shen, PEGylated Elesclomol@Cu(II)-based Metal−organic framework with effective nanozyme performance and cuproptosis induction efficacy for enhanced PD-L1-based immunotherapy, Materials Today Bio 29 (2024) 101317, https://doi.org/10.1016/j.mtbio.2024.101317.

[22] J. Zhang, P. Li, T. Wang, J. Li, K. Yun, X. Zhang, X. Yang, A copper nanocluster-based multifunctional nanoplatform for augmented chemo/chemodynamic/photodynamic combination therapy of breast cancer, Pharmacol. Res. 187 (2023) 106632, https://doi.org/10.1016/j.phrs.2022.106632.

[23] V. Kandathil, S.A. Patil, Single-atom nanozymes and environmental catalysis: a perspective, Adv. Colloid Interface Sci. 294 (2021) 102485, https://doi.org/10.1016/j.cis.2021.102485.

[24] B. Jiang, Z. Guo, M. Liang, Recent progress in single-atom nanozymes research, Nano Res. 16 (2023) 1878–1889, https://doi.org/10.1007/s12274-022-4856-7.

[25] D.-H. Zhao, C.-Q. Li, X.-L. Hou, X.-T. Xie, B. Zhang, G.-Y. Wu, F. Jin, Y.-D. Zhao, B. Liu, Tumor microenvironment-activated theranostics nanozymes for fluorescence imaging and enhanced chemo-chemodynamic therapy of tumors, ACS Appl. Mater. Interfaces 13 (2021) 55780–55789, https://doi.org/10.1021/acsami.1c12611.

[26] D. Jana, D. Wang, A.K. Bindra, Y. Guo, J. Liu, Y. Zhao, Ultrasmall alloy nanozyme for ultrasound- and near-infrared light-promoted tumor ablation, ACS Nano 15 (2021) 7774–7782, https://doi.org/10.1021/acsnano.1c01830.

[27] S. Zhu, B. Zhao, M. Li, H. Wang, J. Zhu, Q. Li, H. Gao, Q. Feng, X. Cao, Microenvironment responsive nanocomposite hydrogel with NIR photothermal therapy, vascularization and anti-inflammation for diabetic infected wound healing, Bioact. Mater. 26 (2023) 306–320, https://doi.org/10.1016/j.bioactmat.2023.03.005.

[28] Q. Xu, Y. Hua, Y. Zhang, M. Lv, H. Wang, Y. Pi, J. Xie, C. Wang, Y. Yong, A biofilm microenvironment-activated single-atom iron nanozyme with NIR-controllable nanocatalytic activities for synergetic bacteria-infected wound therapy, Adv. Healthcare Mater. 10 (2021) 2101374, https://doi.org/10.1002/adhm.202101374.

[29] Y. Wu, Y. Tang, W. Xu, R. Su, Y. Qin, L. Jiao, H. Wang, X. Cui, L. Zheng, C. Wang, L. Hu, W. Gu, D. Du, Y. Lin, C. Zhu, Photothermal-switched single-atom nanozyme specificity for pretreatment and sensing, Small 19 (2023) 2302929, https://doi.org/10.1002/smll.202302929.

[30] Z. Yan, X. Wu, W. Tan, J. Yan, J. Zhou, S. Chen, J. Miao, J. Cheng, C. Shuai, Y. Deng, Single-atom Cu nanozyme-loaded bone scaffolds for ferroptosis-synergized mild photothermal therapy in osteosarcoma treatment, Adv. Healthcare Mater. 13 (2024) 2304595, https://doi.org/10.1002/adhm.202304595.

[31] H. Mai, Y. Wang, S. Li, R. Jia, S. Li, Q. Peng, Y. Xie, X. Hu, S. Wu, A pH-sensitive near-infrared fluorescent probe with alkaline p K_a for chronic wound monitoring in diabetic mice, Chem. Commun. 55 (2019) 7374–7377, https://doi.org/10.1039/C9CC02289A.

[32] D. Jiang, D. Ni, Z.T. Rosenkrans, P. Huang, X. Yan, W. Cai, Nanozyme: new horizons for responsive biomedical applications, Chem. Soc. Rev. 48 (2019) 3683–3704, https://doi.org/10.1039/C8CS00718G.

[33] L. Chen, X. Huang, X. Zeng, G. Fang, W. Chen, H. Zhou, X. Zhong, H. Cai, Signal-on bimodal sensing glucose based on enzyme product-etching MnO2 nanosheets for detachment of MoS2 quantum dots, Chin. Chem. Lett. 32 (2021) 1967–1971, https://doi.org/10.1016/j.cclet.2021.01.030.

[34] M. Huo, L. Wang, Y. Chen, J. Shi, Tumor-selective catalytic nanomedicine by nanocatalyst delivery, Nat. Commun. 8 (2017) 357, https://doi.org/10.1038/s41467-017-00424-8.

[35] L. Lin, J. Song, L. Song, K. Ke, Y. Liu, Z. Zhou, Z. Shen, J. Li, Z. Yang, W. Tang, G. Niu, H. Yang, X. Chen, Simultaneous fenton-like ion delivery and glutathione depletion by MnO_2 -based nanoagent to enhance chemodynamic therapy, Angew. Chem. Int. Ed. 57 (2018) 4902–4906, https://doi.org/10.1002/anie.201712027.

[36] Y. Liu, J. Wang, J. Yang, J. Xia, J. Yu, D. Chen, Y. Huang, F. Yang, Y. Ruan, J.-F. Xu, J. Pi, Nanomaterial-mediated host directed therapy of tuberculosis by manipulating macrophage autophagy, J. Nanobiotechnol. 22 (2024) 608, https://doi.org/10.1186/s12951-024-02875-w.

[37] S. Fan, D. Zhao, J. Wang, Y. Ma, D. Chen, Y. Huang, T. Zhang, Y. Liu, J. Xia, X. Huang, Y. Lu, Y. Ruan, J.-F. Xu, L. Shen, F. Yang, J. Pi, Photothermal and host immune activated therapy of cutaneous tuberculosis using macrophage targeted mesoporous polydopamine nanoparticles, Materials Today Bio 28 (2024) 101232, https://doi.org/10.1016/j.mtbio.2024.101232.

[38] J. Pi, D. Chen, J. Wang, E. Yang, J. Yang, Y. Liu, J. Yu, J. Xia, X. Huang, L. Chen, Y. Ruan, J.-F. Xu, F. Yang, L. Shen, Macrophage targeted graphene oxide nanosystem synergize antibiotic killing and host immune defense for Tuberculosis Therapy, Pharmacol. Res. 208 (2024) 107379, https://doi.org/10.1016/j.phrs.2024.107379.

[39] L. Shen, K. Liao, E. Yang, F. Yang, W. Lin, J. Wang, S. Fan, X. Huang, L. Chen, H. Shen, H. Jin, Y. Ruan, X. Liu, G. Zeng, J.-F. Xu, J. Pi, Macrophage targeted iron oxide nanodecoys augment innate immunological and drug killings for more effective Mycobacterium Tuberculosis clearance, J. Nanobiotechnol. 21 (2023) 369, https://doi.org/10.1186/s12951-023-02103-x.

[40] Y. Li, K. Wang, W. Zhou, Y. Li, R. Vila, W. Huang, H. Wang, G. Chen, G.-H. Wu, Y. Tsao, H. Wang, R. Sinclair, W. Chiu, Y. Cui, Cryo-EM structures of atomic surfaces and host-guest chemistry in metal-organic frameworks, Matter 1 (2019) 428–438, https://doi.org/10.1016/j.matt.2019.06.001.

[41] X. Huang, Q. Chen, Y. Ma, C. Huang, W. Zhi, J. Li, R. Zeng, J. Pi, J. Xu, J. Xu, W. Yang, J. Zhang, H. Cai, J. Zheng, H. Zhou, P. Sun, Chiral Au nanostars for SERS sensing of enantiomers discrimination, multibacteria recognition and photothermal antibacterial application, Chem. Eng. J. 479 (2024) 147528, https://doi.org/10.1016/j.cej.2023.147528.

[42] X. Huang, Z. Zhang, L. Chen, Y. Lin, R. Zeng, J. Xu, S. Chen, J. Zhang, H. Cai, H. Zhou, P. Sun, Multifunctional Au nano-bridged nanogap probes as ICP-MS/SERS dual-signal tags and signal amplifiers for bacteria discriminating, quantitative detecting and photothermal bactericidal activity, Biosens. Bioelectron. 212 (2022) 114414, https://doi.org/10.1016/j.bios.2022.114414.

[43] S.N. Goyal, N.M. Reddy, K.R. Patil, K.T. Nakhate, S. Ojha, C.R. Patil, Y.O. Agrawal, Challenges and issues with streptozotocin-induced diabetes – a clinically relevant animal model to understand the diabetes pathogenesis and evaluate therapeutics, Chem. Biol. Interact. 244 (2016) 49–63, https://doi.org/10.1016/j.cbi.2015.11.032.

[44] M. Schicht, J. Farger, S. Wedel, M. Sisignano, K. Scholich, G. Geisslinger, N. Perumal, F.H. Grus, S. Singh, A. Sahin, F. Paulsen, E. Lütjen-Drecoll, Ocular surface changes in mice with streptozotocin-induced diabetes and diabetic polyneuropathy, Ocul. Surf. 31 (2024) 43–55, https://doi.org/10.1016/j.jtos.2023.12.006.

[45] X. Song, Y. Jiang, F. Cheng, J. Earnshaw, J. Na, X. Li, Y. Yamauchi, Hollow carbon-based nanoarchitectures based on ZIF: inward/outward contraction mechanism and beyond, Small 17 (2021) 2004142, https://doi.org/10.1002/smll.202004142.

[46] D. Saliba, M. Ammar, M. Rammal, M. Al-Ghoul, M. Hmadeh, Crystal growth of ZIF-8, ZIF-67, and their mixed-metal derivatives, J. Am. Chem. Soc. 140 (2018) 1812–1823, https://doi.org/10.1021/jacs.7b11589.

[47] V.B. Saptal, V. Ruta, M.A. Bajada, G. Vilé, Single-atom catalysis in organic synthesis, Angew. Chem. Int. Ed. 62 (2023) e202219306, https://doi.org/10.1002/anie.202219306.

[48] M. Huo, L. Wang, H. Zhang, L. Zhang, Y. Chen, J. Shi, Construction of single-iron-atom nanocatalysts for highly efficient catalytic antibiotics, Small 15 (2019) 1901834, https://doi.org/10.1002/smll.201901834.

[49] J. Pei, R. Zhao, X. Mu, J. Wang, C. Liu, X.-D. Zhang, Single-atom nanozymes for biological applications, Biomater. Sci. 8 (2020) 6428–6441, https://doi.org/10.1039/D0BM01447H.

[50] X. Huang, L. Chen, T. Sha, Y. Lin, R. Zeng, J. Xu, S. Chen, H.-H. Cai, J. Zhang, H. Zhou, P.-H. Sun, X. Jiang, *In situ* tyrosinase monitoring by wearable microneedle patch toward clinical melanoma screening, ACS Nano 17 (2023) 20073–20086, https://doi.org/10.1021/acsnano.3c05638.

[51] X. Huang, L. Chen, W. Zhi, R. Zeng, G. Ji, H. Cai, J. Xu, J. Wang, S. Chen, Y. Tang, J. Zhang, H. Zhou, P. Sun, Urchin-shaped Au–Ag@Pt sensor integrated lateral flow immunoassay for multimodal detection and specific discrimination of clinical multiple bacterial infections, Anal. Chem. 95 (2023) 13101–13112, https://doi.org/10.1021/acs.analchem.3c01631.

[52] G.N. Bosio, D.O. Mártire, Carbon nitride nanomaterials with application in photothermal and photodynamic therapies, Photodiagnosis Photodyn. Ther. 37 (2022) 102683, https://doi.org/10.1016/j.pdpdt.2021.102683.

[53] J. Li, H. Peng, B. Luo, J. Cao, L. Ma, D. Jing, The enhanced photocatalytic and photothermal effects of Ti3C2 Mxene quantum dot/macroscopic porous graphitic carbon nitride heterojunction for Hydrogen Production, J. Colloid Interface Sci. 641 (2023) 309–318, https://doi.org/10.1016/j.jcis.2023.03.015.

[54] X. Huang, B. Sheng, H. Tian, Q. Chen, Y. Yang, B. Bui, J. Pi, H. Cai, S. Chen, J. Zhang, W. Chen, H. Zhou, P. Sun, Real-time SERS monitoring anticancer drug release along with SERS/MR imaging for pH-sensitive chemo-phototherapy, Acta Pharm. Sin. B 13 (2023) 1303–1317, https://doi.org/10.1016/j.apsb.2022.08.024.

[55] D. Pranantyo, C.K. Yeo, Y. Wu, C. Fan, X. Xu, Y.S. Yip, M.I.G. Vos, S. H. Mahadevegowda, P.L.K. Lim, L. Yang, P.T. Hammond, D.I. Leavesley, N.S. Tan, M.B. Chan-Park, Hydrogel dressings with intrinsic antibiofilm and antioxidative dual functionalities accelerate infected diabetic wound healing, Nat. Commun. 15 (2024) 954, https://doi.org/10.1038/s41467-024-44968-y.

[56] Y. Yu, H. Jin, L. Li, X. Zhang, C. Zheng, X. Gao, Y. Yang, B. Sun, An injectable, activated neutrophil-derived exosome mimetics/extracellular matrix hybrid hydrogel with antibacterial activity and wound healing promotion effect for diabetic wound therapy, J. Nanobiotechnol. 21 (2023) 308, https://doi.org/10.1186/s12951-023-02073-0.